symmetry

MDPI

Article

Microcontroller-Based PPF Control of a CFRP–Honeycomb Composite Panel

Antonio Zippo *, Moslem Molaie, Erika Borellini and Francesco Pellicano

Department of Engineering "Enzo Ferrari", Centre InterMech MoRe, University of Modena and Reggio Emilia, 41125 Modena, Italy; moslem_molaie@unimore.it (M.M.); erika.borellini@unimore.it (E.B.); francesco.pellicano@unimore.it (F.P.)

* Correspondence: antonio.zippo@unimore.it

Abstract

In this study, an active vibration control (AVC) strategy is effectively used on a system made of a honeycomb polymer–paper core and carbon fiber-reinforced polymer (CFRP) plates. A cost-effective and practical solution based on an AVC system has been developed and tested using a microcontroller unit (MCU) from Texas Instruments. The control system is studied by applying out-of-plane disturbances to the composite panel via an electrodynamic shaker, by exciting the identified mode shapes obtained through experimental modal analysis, i.e., impact tests. The actuator chosen for the AVC system is a Macro Fiber Composite (MFC) patch. Multiple analog signal processing circuits were developed to scale and shift the signal at the input and output of the MCU. The proposed control algorithm is based on a positive position feedback (PPF) technique. Modal analysis was performed to identify the natural frequencies and mode shapes of the structure, which are essential for the design and tuning of the modal-based PPF controller. This analysis also enabled optimal sensor and actuator placement, ensuring effective targeting and control of the dominant vibration modes. Then, a series of tests were performed using pure sine excitations at frequencies of interest, close to the 2nd and 8th mode at 25.13 Hz and 129 Hz, respectively. The results of the experiments revealed a velocity attenuation of 55.8% to 76.9% and a Power Spectral Density (PSD) attenuation of 5.8 dB to 12.8 dB, depending on the mode under study. Owing to the size and mass properties of the Macro Fiber Composite (MFC) patches, the control system is very much suitable for automobile and aerospace applications.

Keywords: active vibration control system; honeycomb; modal analysis; positive position feedback controller

Academic Editor: Vasilis K. Oikonomou

Received: 12 February 2026
Revised: 20 March 2026
Accepted: 24 March 2026
Published: 30 March 2026

1. Introduction

AVC has been introduced as a technology to manage vibrations in various engineering applications, leveraging advances in control systems. Unlike traditional passive strategies that absorb vibrations without power input, AVC systems employ sensors and actuators to actively counteract unwanted vibrations in real time. AVC has been gaining a lot of attention in the past decade in a wide range of industries. Lee et al. [1] reduced the rotor and airframe vibrations of a helicopter using AVC techniques. They achieved a reduction in vibration of 90% to 98% in a lift-offset compound helicopter when excited with rotary vibrational loads. Testing the performance of the aircraft, the cantilever-like structures are subjected to high vibrations due to their low dynamic stiffness and the effect of the flow field around the aircraft model, leading to discrepancies in the test data. To control the vibration

in this case, Liu et al. [2] used energy-fuzzy adaptive proportional–derivative control to stabilize the structures in subsonic and transonic regimes. Balakrishna et al. [3] developed a wind tunnel active vibration reduction system, which is prone to sting vibration during the test. They used a piezoceramic actuator embedded in the sting to attenuate the modal response even in post-stall conditions, providing an effective solution for sting vibration problems in wind tunnel testing. In 2021, Ma et al. [4] developed a Kalman filter-based control algorithm to control the amplitude of vibrations of an Electrically Controlled Rotor, also called as swashplateless rotor. AVC also aids in the precise functioning of robots, controlling the vibrations induced during the motion of the robot [5]. Wang and Keogh [6] implemented AVC on a 6-axis industrial robot which was used for machining operations to increase the positioning accuracy and surface finish achieved. Jiang et al. [7] used piezo actuators to reduce the relative vibrations between the workpiece and the tool in a milling machine.

The application of AVC in automotive systems imposes strict constraints on compactness and weight, motivating the development of embedded and lightweight control solutions. In this work, a compact AVC implementation based on a 32-bit Texas Instruments (TI) microcontroller is experimentally validated on a carbon fiber-reinforced composite sandwich plate, a material system widely used in automotive and motorsport applications due to its high strength-to-weight ratio. Conventional AVC systems often rely on bulky and expensive laboratory-grade hardware, limiting their suitability for mobile applications. The structural configuration significantly influences the dynamic response of sandwich structures. Ying et al. [8] demonstrated that geometric and material periodicity can be exploited to tune stiffness and damping characteristics. Complementing such structural tailoring, embedded active control strategies provide additional vibration mitigation capability. Previous studies have demonstrated the feasibility of microcontroller-based AVC, including implementations using 8-bit and 32-bit embedded platforms for real-time control applications [9,10].

A wide range of control algorithms have been proposed for AVC, including PID, LQR, position feedback, MPC, neural network-based, and data-driven strategies. Among these, PPF remains attractive due to its simplicity, modal selectivity, and ability to enhance damping around targeted frequencies while limiting spillover. Resonant second-order feedback strategies analogous to PPF have been successfully applied to rotating structures [11] and experimental validations on composite plates using MFC patches have confirmed the robustness and efficiency of PPF under various configurations [12]. More advanced model-based and adaptive approaches have also been investigated, such as RWNN-based control [13], robust H∞/H2 observer-based methods [14], and adaptive iterative learning schemes [15], demonstrating improved performance under nonlinearities and uncertainties. In parallel, optimal sensor–actuator placement strategies have been explored to enhance controllability and reduce control effort [16,17].

Recent studies have extensively explored AVC strategies for smart structures, particularly emphasizing piezoelectric actuation and embedded real-time implementation. These works encompass diverse control algorithms, modeling approaches, and hardware platforms applied to beams, plates, and composite structures. Accurate structural modeling and proper enforcement of boundary conditions are essential for reliable vibration analysis and controller design. For example, Kurpa et al. [18] analyzed the free vibration of porous functionally graded plates using the R-functions method to impose complex boundary conditions without geometric approximations. The importance of nonlinear and stochastic modeling was highlighted by Pellicano and Zippo [19], who reported extreme transient responses in randomly excited cylindrical shells, demonstrating the limitations of purely linear analyses. In smart composite systems, multi-mode suppression using functionally

graded piezoelectric actuators has been demonstrated in MIMO configurations [20], while observer-based and predictive strategies have improved robustness and disturbance rejection [21–23]. Nonlinear actuator modeling and adaptive control schemes have also shown effective vibration attenuation, particularly in MFC-based implementations [22]. More recently, lightweight control algorithms optimized for low-end microcontrollers have confirmed the feasibility of advanced AVC on resource-constrained embedded platforms [24].

In parallel, nonlinear passive and hybrid vibration mitigation strategies have gained attention. High-static–low-dynamic-stiffness (HSLDS) mechanisms have demonstrated substantial transmissibility reduction under harmonic and seismic excitations [25], while origami-inspired quasi-zero stiffness metastructures have shown effective low-frequency isolation [26]. Hybrid active–passive systems integrating microcontroller-driven active components with passive absorbers have further enhanced low-frequency suppression [27]. Additionally, adaptive piezoelectric metamaterials with digital shunt circuits [28], semi-active microcomputer-controlled isolators [29], LPV-based embedded active isolation platforms [30], and microcontroller-based piezoelectric AVC systems for lightweight structures [31] collectively confirm the growing feasibility of real-time embedded vibration control across automotive and aerospace applications.

AVC emerged as a response to the intrinsic limitations of passive damping solutions for lightweight and flexible structures. Passive strategies, including tuned mass dampers or viscoelastic layers provide fixed damping characteristics and often fail to ensure broadband attenuation under varying operating conditions. To overcome these constraints, active control methodologies were developed, relying on real-time sensing and actuation to counteract unwanted vibrations.

The theoretical foundations of AVC were established in the 1970s through state-space control for distributed parameter systems. Within this framework, Balas introduced a rigorous state-space formulation for the control of flexible structures, enabling systematic controller synthesis for distributed vibration systems [32]. Ensuring closed-loop stability in such systems has led to the widespread adoption of collocated actuator–sensor configurations, which inherently mitigate destabilizing spillover from unmodeled high-frequency dynamics; a foundational treatment of modeling and control design for large flexible space structures, emphasizing modal formulations for vibration suppression, is provided in Ref. [33]. Building on this modal control viewpoint, modal positive position feedback can be used to add damping to selected modes and effectively attenuate vibrations in flexible structures, as demonstrated in Ref. [34].

A significant advancement in the development of AVC was the introduction of PPF by Fanson and Caughey [35]. Their work demonstrated that a second-order compensator tuned to a specific modal frequency can substantially enhance modal damping in collocated systems, offering improved robustness and modal selectivity compared to classical proportional or derivative feedback. Subsequent studies examined the stability limitations associated with actuator dynamics and other practical implementation constraints, establishing design guidelines to ensure reliable operation of PPF-based control systems [36].

The introduction of smart materials, and in particular piezoelectric sensors and actuators, enabled integrated sensing and actuation within structural components. Hagood and von Flotow developed coupled electromechanical models for piezoelectric damping, providing the foundation for smart AVC architectures [37]. Later comprehensive treatments consolidated both the theoretical and practical aspects of piezoelectric vibration control, addressing implementation issues, robustness considerations, and design methodologies for reliable smart AVC systems [38,39].

Extensions of classical PPF strategies included modified formulations to enhance damping performance in lightly damped systems [40] and multi-modal PPF approaches

capable of suppressing multiple resonances simultaneously [41]. In parallel, adaptive and hybrid control strategies were developed to improve robustness under parameter uncertainty and time-varying dynamics [42,43].

With the rapid evolution of embedded processing platforms, practical implementation aspects such as sampling delays, discretization effects, quantization errors, and computational limitations became central considerations in AVC system design. Foundational contributions in active vibration and noise control addressed both theoretical and digital implementation challenges, establishing guidelines for real-time realization on resource-limited hardware platforms [44,45]. Beyond classical control developments, recent research in structural dynamics has highlighted the role of geometric symmetry and structural configuration in vibration behavior. Structural symmetry simplifies modal decomposition, clarifies modal coupling patterns, and can reduce computational effort in finite element analyses. Exploiting symmetry properties and modal strain energy distribution has also been shown to support improved actuator placement and controllability assessment in composite and sandwich structures. These contributions reinforce the importance of accurate structural modeling and modal characterization as a prerequisite for effective active vibration suppression and illustrate how geometric symmetries simplify modal and dynamic analysis of structures, which indirectly supports the understanding of symmetry in vibration design [46], while covering symmetry considerations in structural health monitoring, including vibration characteristics [47]. Taken together, these contributions outline the scientific and technological framework within which modern embedded PPF-based AVC systems are situated.

In this study, an embedded AVC framework based on PPF is developed and experimentally validated on a composite honeycomb sandwich plate, extending the preliminary results published in Ref. [48]. The main novelty of this work lies in the complete system-level implementation and experimental validation of a PPF-based active vibration control strategy on a low-cost microcontroller platform, demonstrating performance comparable to laboratory-grade real-time systems. PPF is selected for its simplicity and suitability for real-time implementation with minimal setup complexity. The proposed system integrates a microcontroller-based controller with surface-bonded Macro Fiber Composite (MFC) patches acting as collocated sensor–actuator pairs. The procedure begins with modal identification and finite element analysis to determine the dominant vibration mode and optimal actuator placement based on modal strain energy distribution. The PPF compensator is subsequently designed and discretized for implementation on a resource-constrained microcontroller, with attention to sampling requirements and numerical stability. Dedicated analog signal-conditioning circuits interface the piezoelectric elements with the embedded platform to ensure proper scaling and signal integrity. The overall control architecture is validated experimentally under harmonic excitation, demonstrating the feasibility and practicality of microcontroller-based AVC for lightweight composite structures.

2. Materials and Methods

Most of the experiments found in the literature on AVC were conducted in a laboratory wherein a real-time data acquisition system like dSPACE (MicroLabBox with DS1202 PowerPC DualCore 2 GHz processor board and DS1302 I/O board, Paderborn, Germany) was used. The idea proposed in this study is to substitute the acquisition system with a microcontroller unit (MCU). This approach presents both advantages and limitations. The main limitation lies in the reduction in control resulting from the lower resolution and processor speed of the MCU. Nevertheless, the use of an MCU represents a practical and feasible solution for the intended application. Because of the size and weight of the

MCU, it is a more suitable candidate for AVC implementation in both automobiles and aerospace structures.

The microcontroller imposed stringent constraints on the resolution of the analog-to-digital converter (ADC), wherein the data acquisition system typically used in this application operates with 64-bit ADC resolution. Therefore, the MCU should incorporate an ADC with the highest possible resolution to achieve accuracy and precision comparable to those of the dSPACE data acquisition system, while still preserving the compactness of the MCU board. Additional constraints included the need for a higher clock speed, a higher ADC sampling frequency, an integrated DAC, and MATLAB R2024a and Simulink R2024a compatibility. Microcontrollers from Arduino, Texas Instruments and STMicroelectronics were identified as strong contenders for the application. Considering the three microcontrollers, see Table 1, the Texas Instruments (Dallas, TX, USA) TI C2000's TMS320F2837xD LaunchPad was selected because of its higher clock speed and its higher-resolution ADC. The computational demand of the implemented PPF controller is minimal, as it consists of a second-order discrete filter requiring only a small number of floating-point operations per sampling interval. Running on the 200 MHz C28x core of the TMS320F28379D [49], the estimated computational load remains well below 1% of the available processing capacity. In terms of power consumption, the microcontroller operates with a typical core power of approximately 0.5–0.7 W.

Table 1. Comparison of MCUs from Arduino, Texas Instruments and STMicroelectronics.

Parameters	Arduino Due	TI TMS320F2837xD	STM32F373C8
Clock speed (MHz)	84	200	72
ADC resolution (bits)	12	12/16	12/16
Number of ADC channels	12	24 in 12-bit mode; 12 in 16-bit mode	21 in 12-bit mode; 11 in 16-bit mode
DAC resolution (bits)	12	12	12
Number of DAC channels	2	3	3
Compatibility with Simulink	Yes	Yes	Yes

2.1. Interfacing MCU with Simulink

The C2000 MCU is connected with the PC via serial communication. The embedded coder support package for Texas Instruments C2000 processors in MATLAB generates ANSI/ISO C/C++ code which can be subsequently complied and deployed on the TI C2000 MCUs using the Code Composer Studio IDE 2020, provided by Texas Instruments. Embedded coder allows the code generated from Simulink algorithms to manage software interfaces, optimize the implementation, and minimize memory usage. The embedded coder support package also provides automated code building and execution, together with dedicated libraries, and it also supports real-time parameter regulation and tuning.

2.2. Analog-to-Digital Signal Processing Circuits

The ADCs integrated in the TI device adopt a successive approximation register (SAR) architecture with selectable resolution of 16 bits, with differential input, or 12 bits, with single-ended inputs. Multiple ADC modules are available, enabling simultaneous sampling. The ADC wrapper is start-of-conversion (SOC)-based. The sensors employed in the system produce output signals ranging from −10 V to +10 V, whereas the ADC inputs of the MCU should be in the range of 0 V to +3 V. For this reason, dedicated signal-conditioning circuitry was implemented to match the sensor output to the microcontroller's input range. Specifically, a resistive voltage divider was first employed Figure 1a to scale the voltage amplitude of sensors from ±10 V up to ±1.37 V (Equation (1)). Subsequently, a

non-inverting summing amplifier Figure 1b was placed in series to provide the required DC offset while maintaining a unity gain, ensuring that no amplification was added to the signal. This configuration shifts the scaled waveform by 1.5 V, resulting in a final signal confined within the MCU's allowable 0–3 V input window.

$$V_{out} = \frac{R_2}{R_2 + R_1} \cdot V_{in} \tag{1}$$

$$\begin{gathered} A_v = 1 + \frac{R_4}{R_3} \approx 1.122 \\ V_p = V_p{}' + V_p{}'' = V_{in} \frac{R_2}{R_1 + R_2} + V_1 \frac{R_1}{R_1 + R_2} \\ V_{out} = A_v \cdot V_p \end{gathered} \tag{2}$$

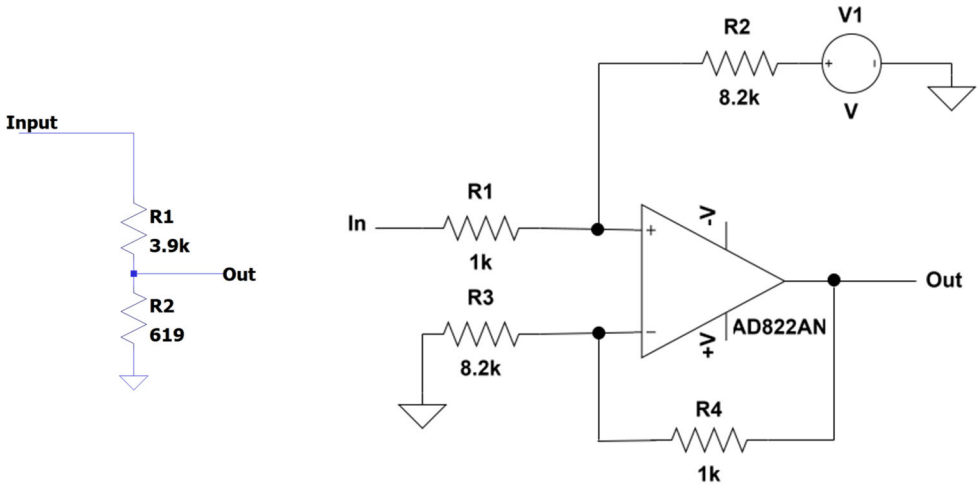

(**a**) (**b**)

Figure 1. (**a**) Resistive voltage divider, (**b**) non-inverting summing amplifier.

The circuits were designed in the Simulink environment, shown in Figure 2, and then implemented on solderable prototyping boards, as shown in Figures 3 and 4.

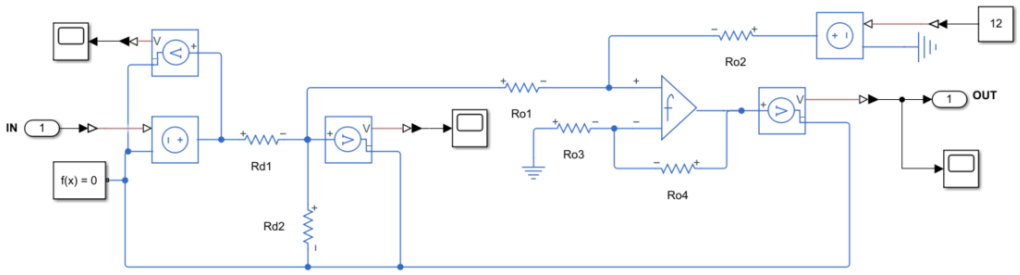

Figure 2. Simulink diagram of resistive voltage divider and non-inverting summing amplifier.

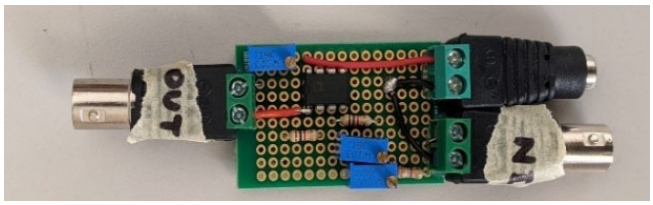

Figure 3. Signal processing circuit (SPC) at input of ADC in 12-bit mode, called Input-SPC.

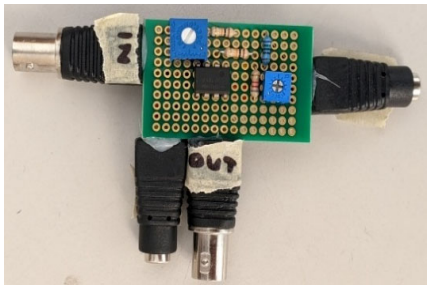

Figure 4. Signal processing circuit (SPC) at output of DAC, called Output-SPC.

In addition to the previous implemented circuits, since the TI device integrates SAR ADCs that operate in differential mode, an additional circuit is required to generate the complementary inputs ADCINxN and ADCINxP (see Ref. [19]) and establish the ADC's required common voltage (Equation (3)).

$$V_{CM} = \frac{\text{ADCINxN} + \text{ADCINxP}}{2} \tag{3}$$

A fully differential amplifier, seen in Figures 5 and 6 and Table 2, from Linear technology-LTC6362 (Milpitas, CA, USA) is employed. The LTC6362 is a low-power, low-noise differential amplifier with rail-to-rail input and output swing, specifically optimized to drive low-power successive-approximation (SAR) ADCs.

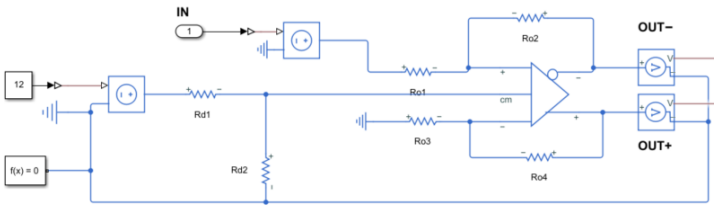

Figure 5. Simulink block diagram illustrating the circuit needed at the input of the MCU when operating the ADC in 16-bit mode.

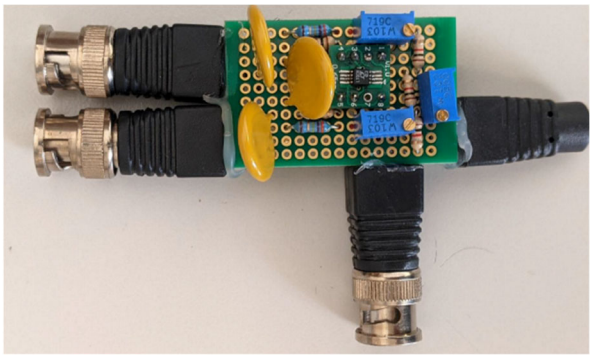

Figure 6. Realized circuit related to Figure 5 with the addition of three 3.9 nF capacitors to minimize voltage fluctuations, providing a low-impedance path for parasitic currents.

Table 2. Resistances used in the circuit of Figure 5.

	Resistance [Ω]
Rd_1	3300
Rd_2	490
Ro_1	3300
Ro_2	1000
Ro_3	3300
Ro_4	1000

The amplifier is configured to convert a single-ended sensor output signal from the preceding conditioning stages into a differential, non-inverting output. The amplifier produces complementary outputs (OUT+ and OUT−), which form the differential pair required by the ADC. The amplifier common-mode pin is biased to a constant 1.5 V, using a resistive voltage divider network powered at 12 V supply, in order to guarantee that both amplifier outputs remain inside the ADC input window.

$$\delta = \frac{\mathrm{d_{33}V} + \dfrac{\mathrm{F}}{\mathrm{K_a}}}{1 + \dfrac{\mathrm{K}}{\mathrm{K_a}}} \tag{4}$$

$$V_{node} = \frac{Rd_2}{Rd_2 + Rd_1} \cdot V_{in} = \frac{490}{490 + 3300} \cdot 12 = 1.5\ \mathrm{V} \tag{5}$$

The feedback and input resistors were chosen for the required differential gain while preserving symmetry. Specifically, Ro_2 and Ro_4 act as feedback resistors and determine the closed-loop gain, together with Ro_1 and Ro_3, where the gain is established by the ratio $\mathrm{A_1} = Ro_2/Ro_1$ and $\mathrm{A_2} = Ro_4/Ro_3$. $\mathrm{A_1}$ and $\mathrm{A_2}$ are equal to guarantee the symmetry.

2.3. Macro Fiber Composite (MFC) Patches

The proposed control system in this study focused on developing a lightweight and portable system. To meet the requirements, smart materials were considered as an ideal choice for actuators. Macro Fiber Composites (MFCs) are composed of rectangular piezoceramic fibers embedded between layers of adhesive, electrodes, and polyimide films. The electrodes, patterned in an interdigitated configuration on the polyimide layers, enable efficient transfer of the applied electric field directly to and from the ribbon-shaped fibers. This architecture allows in-plane poling and facilitates both actuation and sensing within a sealed and mechanically robust package. When an electric voltage is applied, the MFC operates as an actuator, inducing bending or deformation in the host structure, enabling vibration generation, or actively suppressing structural vibrations. In the absence of an applied voltage, it can work as a highly sensitive strain gauge sensor capable of detecting deformations, noise, and vibrations. Different types of MFC patches are available based upon the behavior of the patches under an applied voltage. The MFC P1 type, which works on the $\mathrm{d_{33}}$ effect [12], is chosen for this application. The $\mathrm{d_{33}}$ effect is achieved through the stacked arrangement of the piezoelectric material. In this configuration, the piezoelectric stacks are arranged such that the application of a voltage across the electrodes induces a longitudinal extension of the stack, commonly referred to as operation along the 3–3 axis. This characteristic makes stacked piezoelectric actuators particularly suitable for applications in vibration isolation. For a given applied voltage V, the resulting net static displacement δ of a piezoelectric ceramic actuator configured in parallel can be expressed as

$$\delta = \frac{d_{33}V + \dfrac{F}{K_a}}{1 + \dfrac{K}{K_a}} \tag{6}$$

where $\mathrm{d_{33}}$ is the strain constant of the piezoelectric material in the 3-3 axis, K is the external spring stiffness, K_a is the actuator stiffness ($K_a = E_a A_a / L_a$, where E_a, A_a, and L_a are the actuator's young's modulus, cross-sectional area, and length, respectively). F is the external load force.

The advantage of piezoelectric stack, compared with other configurations such as piezoelectric wafers, is its ability to provide high force. However, this comes at the expense

of a limited displacement range. The P1-type patches elongate up to 1800 ppm if operated at maximum voltage range of −500 V to +1500 V. When subjected to an oscillating voltage, the patch oscillates at the same frequency as the input.

The thin rectangular MFC patches, produced by Smart Materials Corp (Dresden, Germany), were bonded using an epoxy glue, while the electric connections were made by soldering the wires directly to the patches, which can be used both as actuators or sensors; in our study, two different sizes were used separately as actuators (M8557-P1) and sensors (M8507-P1). The same properties for both patches are shown in Table 3.

Table 3. Dimensions and electrical properties of MFC patches.

	M8507-P1	M8557-P1
Active length [mm]	85	85
Active width [mm]	7	57
Overall length [mm]	101	103
Overall width [mm]	13	64
Capacitance [nF]	3.1	16
Free strain [ppm]	1035	1350
Blocking force [N]	65	693

2.4. Signal-Conditioning Hardware: Voltage Amplifier

In this work, the output of the DAC of the TI F28379D board ranges from 0.3 V to 3 V, while the MFC actuators operate on a voltage range of −500 V to +1500 V. Therefore, a TREK high-voltage power amplifier (model PA05039, see Table 4 and Figure 7) was employed to provide the necessary gain (×200). The PA05039 accepts an input range between −2.5 V to + 7.5 V; consequently, an additional analog conditioning circuit stage was implemented to scale and offset the output of the DAC to a voltage range of −2.5 V to +7.5 V, such that the required level of shift and gain is achieved and the DAC can be used as the low-voltage command source for the high-voltage amplifier.

Table 4. Specifications of the voltage amplifier.

Parameter	Value
Input voltage range	−2.5 V to +7.5 V DC or peak AC
Input impedance	25 kΩ nominal
Output voltage range	−500 V to +1500 V
Output current range	0 to ±35 mA DC 0 to ±50 mA peak AC
DC voltage gain	200 v/v (non-inverting)
Offset voltage	Less than 1 V
Slew rate (10% to 90%)	Greater than 50 V/µs

Figure 7. Voltage amplifier used after the MCU.

To accomplish the aforementioned goals, in Figure 8 is represented the employed circuit including the resistive voltage divider supplied from a 12 V source which provides the bias node used to generate the offset, while in Figure 9 the signal processing circuit implementation is shown. The bias is summed with the input signal to produce the required DC shift prior to amplification. The resistance data is reported in Table 5.

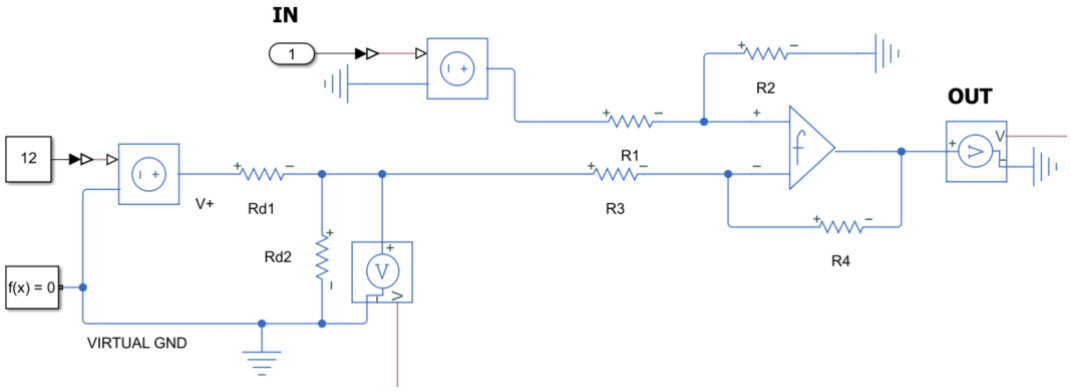

Figure 8. Simulink block diagram to meet the requirements of the actuators.

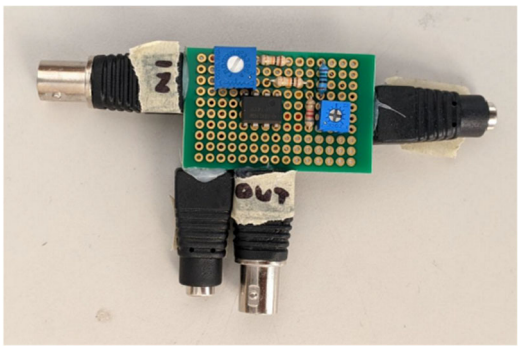

Figure 9. Signal processing circuit represented in the schematic of Figure 8.

Table 5. Resistances used in Figure 8.

	Resistance [Ω]
Rd_1	8200
Rd_2	950
R_1	460
R_2	8400
R_3	8400
R_4	27000

2.5. Positive Position Feedback Control Algorithm

PPF control is one of the most commonly used algorithms for resonant control techniques. Its working principle is explained as follows: consider a single-degree-of-freedom system with a single decoupled mode, as represented by the following equation:

$$\ddot{q}(t) + 2\zeta\omega_n\dot{q}(t) + \omega_n^2 q(t) = g\omega_n^2\eta \tag{7}$$

where ζ is the damping ratio and ω_n is the natural frequency of the structure. g is the plant gain, $\dot{\eta}$ is the compensator output, which is the position of compensator. q is the position

of the structure under study. The PPF controller is modeled as a second-order dynamic system, which is represented by the following equation:

$$\ddot{\eta}(t) + 2\zeta_c\omega_c\dot{\eta}(t) + \omega_c^2\eta(t) = kq\omega_c^2 \tag{8}$$

where ζ_c is the damping ratio of the compensator, ω_c is the frequency of the compensator and k is the compensator gain. The stability of the PPF controller is found by combining the above two equations, limiting them to a second-order level and assuming no external forces on the structure:

$$\begin{Bmatrix} \ddot{q} \\ \ddot{\eta} \end{Bmatrix} + \begin{bmatrix} 2\zeta\omega_n & 0 \\ 0 & 2\zeta_c\omega_c \end{bmatrix} \begin{Bmatrix} \dot{q} \\ \dot{\eta} \end{Bmatrix} + \begin{bmatrix} \omega_n^2 & -g\omega_n^2 \\ -k\omega_c^2 & \omega_c^2 \end{bmatrix} \begin{Bmatrix} q \\ \eta \end{Bmatrix} = \begin{Bmatrix} 0 \\ 0 \end{Bmatrix} \tag{9}$$

The PPF controller is stable if the stiffness matrix is positive definite, that is, the eigenvalues are all positive.

$$\begin{gathered} \left(\omega_n^2\right)\left(\omega_c^2\right) - \left(-g\omega_n^2\right)(-k)\left(\omega_c^2\right) > 0 \\ gk < 1 \end{gathered} \tag{10}$$

The compensator implies active damping if η is -90° out of phase with respect to q at ω_n. It adds active flexibility at lower frequencies and active stiffness at higher frequencies. Therefore, the compensator is usually turned at $\omega_c = \omega$, in order to have the desired attenuation of the amplitude of vibration. The transfer function takes the form of Equation (10).

$$H(s) = \frac{\omega_c^2}{s^2 + 2\zeta_c\omega_c s + \omega_c^2} \tag{11}$$

At frequencies higher than the cutoff value ω_c, the magnitude of the transfer function decreases sharply, exhibiting a roll-off of approximately -40 dB per octave. This steep attenuation mitigates spillover effects associated with high-frequency vibration modes. In contrast, for frequencies below ω_c, the magnitude of the transfer function H(s) remains close to 0 dB, a condition that may promote spillover phenomena. In this context, spillover refers to unintended interactions whereby the control sensor detects non-target modes and the actuator inadvertently excites them, an effect that is particularly pronounced when sensors and actuators are located in close proximity. Under these conditions, the effective damping ratio of the controlled system can be expressed as

$$\zeta_s = \zeta + \frac{g}{4\zeta_c} \tag{12}$$

Equation (12) illustrates the damping augmentation effect introduced by the PPF controller. When the compensator is tuned close to the natural frequency of the targeted mode, the closed-loop dynamics can be approximated by a second-order system in which the effective modal damping is increased by the additional term $\frac{g}{4\zeta_c}$. This relationship highlights that the vibration suppression performance is primarily governed by the appropriate selection of the controller gain and damping parameters, wherein the parameters g and ζ_c must be selected with care, as they directly shape the resulting Bode response of the closed-loop system. Compared with negative position feedback, PPF demonstrates superior robustness against high-frequency spillover. Specifically, the asymptotic decay rate of the PPF transfer function follows a $1/\omega^2$, trend, whereas negative feedback exhibits a slower $1/\omega$ roll-off. Although PPF is typically recommended for lightly damped structures with well-separated modes, in the present study it is shown to effectively attenuate spillover effects originating from modes beyond the targeted frequency range. Extending modally optimized control strategies to nonlinear vibration regimes requires

accounting for frequency shifts due to hardening or softening behavior, as well as the emergence of subharmonic, superharmonic, and combination resonances. A commonly adopted approach involves the use of a linearization stage followed by a conventional linear control algorithm. Alternatively, a PPF-based controller can directly accommodate weak nonlinearities without explicit linearization.

The selection of the PPF parameters was carried out using a modal-based tuning strategy. The compensator natural frequency was set close to the experimentally identified natural frequency of the targeted mode, ensuring effective damping augmentation in the vicinity of resonance. The compensator damping ratio was chosen to provide a well-conditioned second-order response, balancing vibration attenuation and stability while limiting excessive amplification near the tuned frequency. The controller gain was initially selected based on stability considerations derived from the closed-loop formulation and then refined experimentally through real-time tuning in the Simulink environment. The gain was gradually increased until significant vibration attenuation was achieved without inducing instability or noticeable spillover effects. The gain selection was performed experimentally to maximize attenuation while preserving stable behavior, consistent with the practical tuning approach used in industrial implementations, where, in general, a systematic gain-sensitivity map that represents the attenuation and stability versus gain is required when the controller must operate across a wide range of operating conditions.

As a resonant, mode-selective controller, PPF effectiveness is maximized when the compensator frequency is aligned with the targeted modal frequency. The experimental results reported in this work therefore correspond to the tuned configuration adopted for the selected mode. For applications where the modal frequency can drift, due to temperature or boundary-condition variations, a detuning-robustness characterization, around 1–2% of the selected mode, is a natural extension.

This combined analytical–experimental procedure allowed effective suppression of the selected mode while preserving robust closed-loop behavior; the stability is supported analytically by the positive-definiteness condition of the closed-loop stiffness matrix and all eigenvalues are strictly positive, which provides a direct stability criterion within the adopted reduced-order coupled formulation.

A classical gain/phase margin analysis would require a dedicated loop model identification consistent with the implemented digital controller and is beyond the scope of this experimental validation.

For a multi-degree-of-freedom structure, the practical implementation of PPF control is governed by

$$\begin{aligned} M\ddot{x} + C\dot{x} + Kx &= C_a v_a \\ v_s &= C_s x \end{aligned} \tag{13}$$

where M, C, and K denote the mass, damping, and stiffness matrices, respectively; x is the physical displacement vector; v_a and v_s are the actuator and sensor voltage vectors; and C_a and C_s represent the actuator and sensor participation matrices. Introducing a reduced-order modal representation,

$$x = Uq \tag{14}$$

with q denoting the generalized modal coordinates and U the matrix of eigenvectors, the system equations can be rewritten in reduced modal form as

$$\begin{aligned} \ddot{q} + 2Z\Omega\dot{q} + \Lambda q &= \overline{B_a} v_a \\ v_s &= \overline{C_s} x \end{aligned} \tag{15}$$

For real-time embedded implementation, the PPF controller originally designed in the continuous domain as a second-order resonant filter was discretized within the Simulink environment and deployed to the TI F28379D microcontroller using embedded coder with a fixed-step discrete solver. The control loop operates with a constant sampling period corresponding to the selected sampling frequency (4096 Hz), forming a deterministic sequence of SAR-based ADC acquisition, discrete PPF computation, and DAC-based actuation. The sensor signal is acquired through the onboard SAR ADC configured in 12-bit mode, for single-ended input [49], while the discrete PPF algorithm runs in floating-point arithmetic on the C28x core, thus avoiding fixed-point truncation effects in the control computation. To mitigate quantization effects and prevent saturation of the DAC or high-voltage amplifier during tuning, a pre-filter gain was introduced to scale the measured signal to the normalized range expected by the controller and to limit the overall loop gain. This gain was determined experimentally to achieve maximum vibration attenuation without introducing saturation or instability in the closed-loop system.

2.6. Honeycomb Carbon Fiber Sandwich Panels

Carbon fiber honeycomb sandwich panels are inevitable in the high-performance automotive industry, motorsports, and aerospace applications. The plate is made up of two stiff outer skins of carbon fiber with a low-density, low-stiffness inner core of polymer honeycomb. The outer skin of the composite plate is made up of carbon/epoxy composite with a 0/90° lay-up, wherein each layer has a thickness of 0.17 mm. The plate's properties have been identified using static and dynamic tests. The inner core is made of PLASCORE PN2 aramid fiber paper and DuPont Nomex paper, with hexagonal cell dimensions L = H = 4.5 mm, t = 0.0762 mm, and θ = 30° and an average 2.92 mm core thickness. The plate was divided into 54 points, 6 columns and 9 rows, and each point was analyzed during experimental modal analysis using the impact hammer. The plate is attached to a rigid frame using bungee cords to keep the plate in position. During the test performed, the attachment points had to be reviewed because of observed inconsistencies at low frequencies. The observed effect was due to the too-short wires used for connecting the plate with the support and hence the plate was not freely suspended. Hence, at lower frequencies, the system behaves as one. The specifications of the plate are mentioned in Table 6.

Table 6. Specification of CFRP plate.

Property	Specification
Designation of carbon composite	GG285P(T700)-DT 120-40 (H 100 cm)
Designation of polymer	NOMEX
Polymer thickness	3 mm
Plate dimensions	1000 mm × 500 mm

The properties of the carbon fiber fabric used are given in Table 7.

Table 7. Specification of the carbon fiber fabric used.

Parameter	Value
Yarn type	Toray T700 12K
Weaving style	Plain
Standard width	1000 ± 5 mm
Standard length	50 ± 5 m
Warp (ends/cm)	1.80 ± 0.1

Table 7. *Cont.*

Parameter	Value
Weft (picks/cm)	1.80 ± 0.1
FAW	285 ± 15 g/m^2
Resin content	40 ± 3% by weight
Volatile content	<1% by weight
Laminate thickness	0.31 mm

2.7. Shaker

To conduct the study from a control perspective, the composite sandwich plate was excited using an electrodynamic shaker (TIRAvib S 502, Schalkau, Germany), to provide controlled and repeatable out-of-plane disturbances for modal identification and closed-loop tests. The shaker is characterized by a rated peak force of 18 N and operates over a wide frequency range from 2 Hz to 10 kHz, making it suitable for the excitation of low-frequency flexible modes of the structure. The shaker allows a maximum sinusoidal velocity of 0.8 m/s and a rated travel of 5 mm, ensuring sufficient excitation authority without inducing mechanical nonlinearities. The excitation force was measured using a force transducer, and a steel stinger was employed to connect the transducer to the plate in order to minimize misalignment and transverse loading. The shaker input signal was generated through the experimental control chain and used consistently throughout both the identification and control experiments.

2.8. Laser Vibrometer

The out-of-plane vibration response of the composite sandwich plate was measured using a laser Doppler vibrometer (Polytec OFV-505, Waldbronn, Germany), interfaced with an OFV-5000 vibrometer controller. The non-contact nature of the measurement eliminates mass loading effects and avoids mechanical interference with the structure, which is particularly important for lightweight composite plates. The vibrometer output signal was routed through the experimental control chain and synchronized with the excitation and control signals, allowing precise time- and frequency-domain analysis of the structural response.

3. Experimental Setup

The locations of the sensor and actuator are crucial parameters for achieving effective control. The placement of sensor and actuator depends on the mode shape to be controlled, considering that the PPF algorithm is a modal-based algorithm, implying the need to input the natural frequencies of the structure into the transfer function of the algorithm. Hence an experimental modal analysis using impact testing was used to find the natural frequencies and mode shapes of the CFRP plate under study.

3.1. Experimental Modal Analysis

The test setup for experimental modal analysis is outlined in Table 8 and Figure 10. A monoaxial piezoelectric accelerometer (DYTRAN 3035B (Chatsworth, CA, USA), sensitivity: 98.8 mV/g; range: 0.5 to 10 k Hz) and an ICP impact hammer 086C01 (sensitivity: 11.2 mV/N; range: $\pm$444 N) are connected to the data acquisition system using shielded cables and BNC connectors.

Table 8. Test parameter values.

Test Parameters	Value
Trigger level	0.0053 V
Pre-trigger delay	0 s
Bandwidth	512 Hz
Resolution	0.5 Hz
Acquisition time	2 s
Number of spectral lines	1024

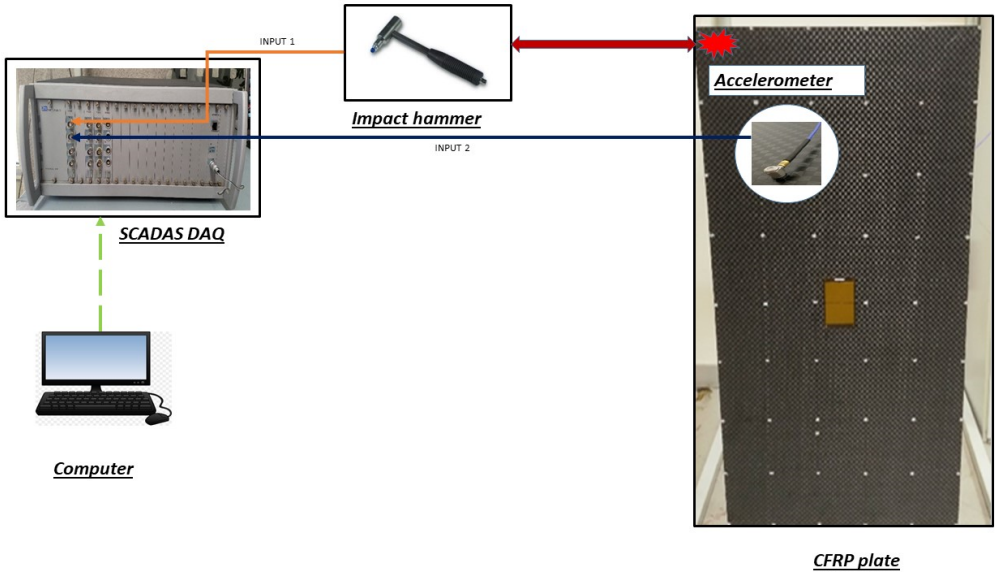

Figure 10. Test setup.

Three measurements were averaged for each of the 54 defined points. A total of twenty-four modes has been identified in the frequency range of 0 to 512 Hz. The first three modes correspond to rigid body modes. The two selected modes for the application of active vibration control are at 25.13 Hz and 132 Hz, which are shown in Figure 11, respectively. These two modes fall within the frequency range of interest and they can be controlled with a single-input–single-output osystem, hence requiring on sensor and one actuator. Moreover, selecting which natural frequencies to control—and the corresponding mode shapes—is a crucial step when using a positive position feedback controller. The actuator should not distort the target mode shape that the controller is designed to suppress: in our case, the actuation is provided by piezoelectric patches. When the patches expand and contract along their in-plane longitudinal direction (i.e., along the long side of the patch), they generate a bending action, out of plane, that induces curvature in the plate. Therefore, the control action is intrinsically related to the local curvature field associated with each vibration mode. In modal coordinates, the effectiveness of the positive position feedback controller depends on the modal participation factor, which quantifies the projection of the actuator-induced bending distribution onto the corresponding mode shape. Modes exhibiting significant curvature and strain energy concentration in the region covered by the patches provide large controllability coefficients and enable efficient energy exchange with the controller. Conversely, modes characterized by negligible curvature or nodal lines within the actuator area are weakly controllable and only marginally affected by the feedback action. For this reason, the selected vibration modes are chosen specifically to satisfy this deformation constraint. This spatial compatibility ensures that the control action

predominantly augments the modal damping of the targeted modes. At the same time, the limited projection onto non-selected modes mitigates spillover effects and preserves modal orthogonality. As a result, the controller can effectively attenuate the disturbance without altering the intrinsic dynamic behavior of the structure, maintaining the original modal stiffness and mass characteristics while increasing dissipation in the controlled subspace.

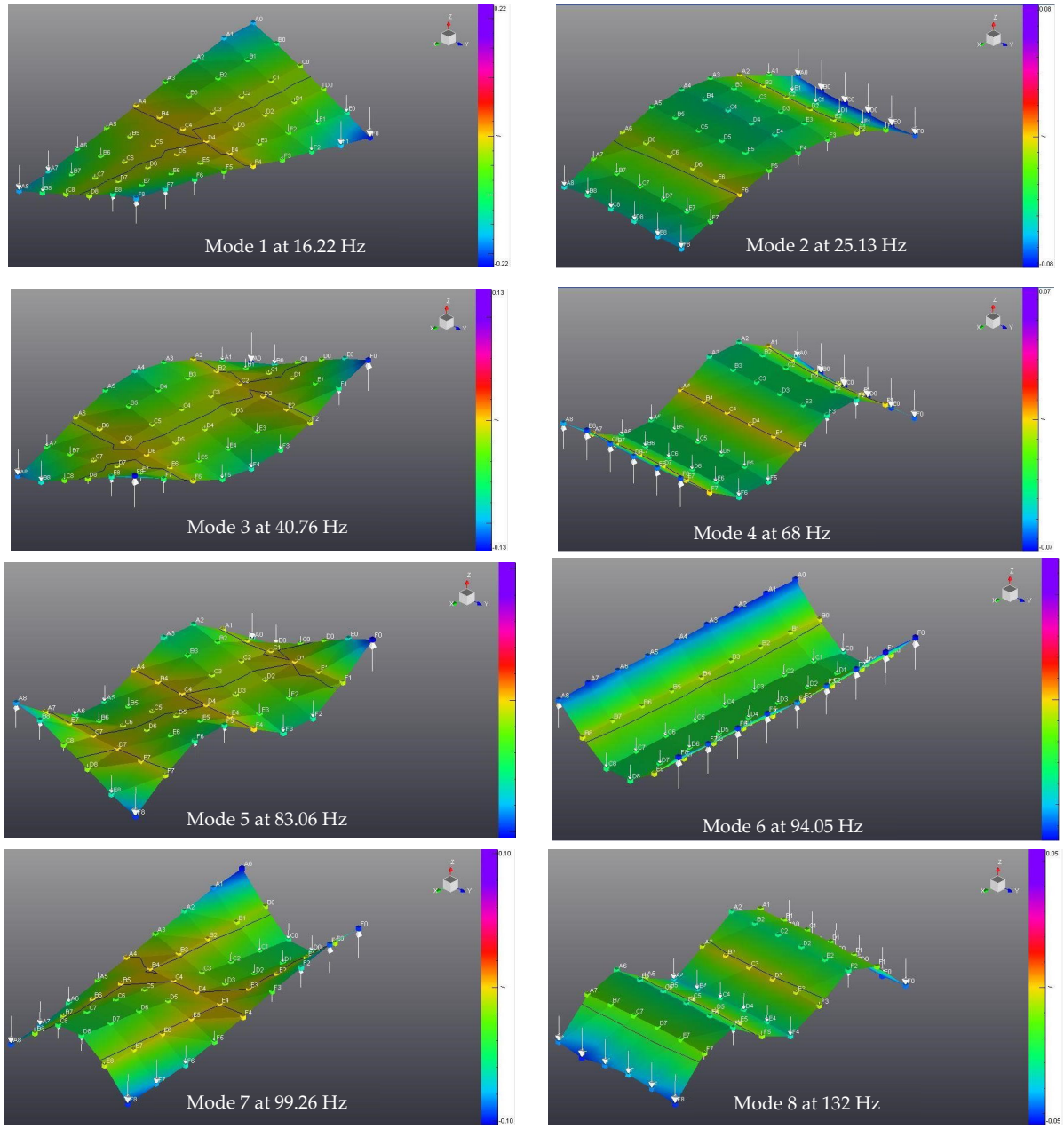

Figure 11. Results of modal analyses done by impact test.

3.2. Experiments on Active Vibration Control

The system under investigation is a 3 mm thick composite plate made of carbon fiber honeycomb sandwich panels. The plate is excited using an electrodynamic shaker, with the excitation point located at (165 mm, 250 mm) with respect to the lower-left corner of the plate. A harmonic steel stinger is placed between the shaker and the transducer in order to minimize misalignment and transverse force components. The vibration response of the plate is measured using a laser Doppler vibrometer. The selected measurement point is

located at the center of the actuator patch, as shown in Figure 12. The control algorithm is implemented on the TI LAUNCHXL-F28397D microcontroller unit (MCU).

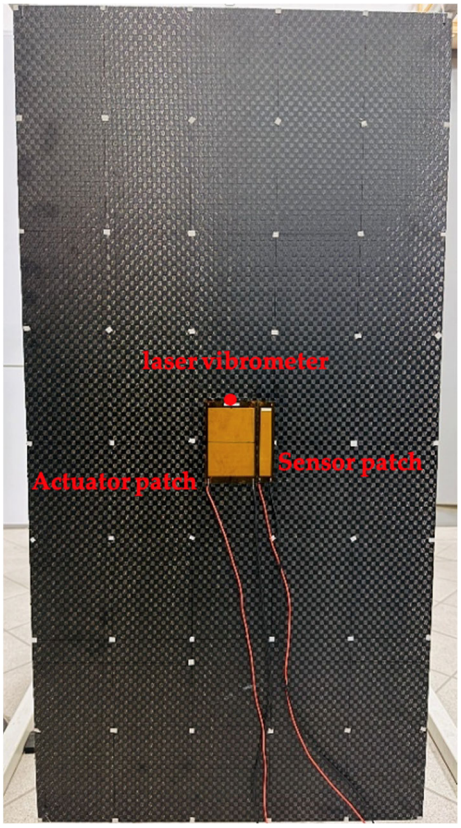

Figure 12. The plate with actuator and sensor patch.

Two experimental configurations are investigated using the microcontroller: case 1,2 and 3, see Figure 13. In case 1 and 2, the laser vibrometer signal is used as the input to the controller. In case 3, the M8507-P1 Macro Fiber Composite (MFC) patch is used as a sensor and provides the input to the controller. In this latter configuration, the M8507-P1 patch is placed close to the actuator and connected to the MCU through a custom-designed analogic signal-conditioning circuit, which scales the voltage signal to remain within the acceptable limits of the analog-to-digital converter (ADC). In both configurations, the output of the laser vibrometer is used to monitor the plate response. The MCU is interfaced with the Simulink environment, allowing real-time tuning of the controller gain. The PPF algorithm is deployed on the flash memory of CPU1 using Simulink embedded coder. The output signal generated by the MCU is sent to a high-voltage power amplifier and then applied to the M8557-P1 MFC patch, which acts as the actuator, through the designed analogic signal-conditioning circuit. This setup constitutes a closed-loop control system on which the experimental tests are conducted. The closed-loop control architecture is illustrated in Figure 13. In the first configuration, when the vibrometer is used as the controller input, the green arrow indicates the signal path to the MCU for test case 1 and 2. In the second configuration, the vibrometer is used only for response measurement, while the controller input is provided by the MFC sensor patch, i.e., test case 3. An additional test case (case 4) was performed in order to compare the results: the same algorithm used within the microcontroller was deployed on a dSPACE control platform.

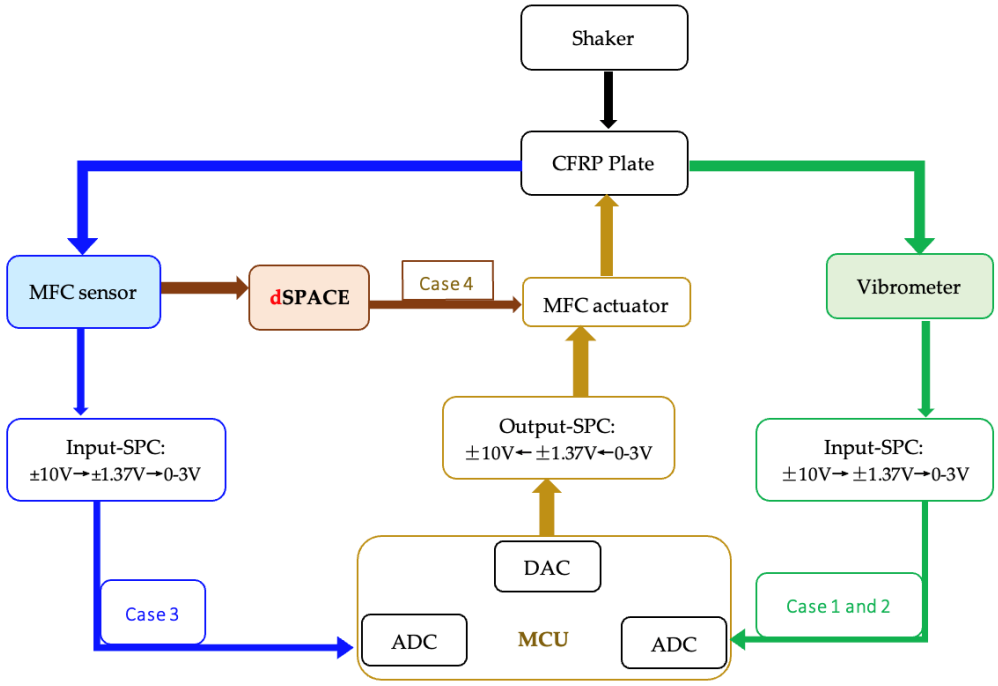

Figure 13. Closed-loop control system scheme.

4. Experimental Results

This section investigates the experimental cases of active vibration control under pure-tone sine wave excitation. In the first case, the shaker applies a harmonic disturbance at 129 Hz, close to the structure's natural frequency, that is controlled using a laser vibrometer as the input sensor. The second case focuses on control at 25.13 Hz, where the controller is reconfigured to target a lower-frequency mode while still using the vibrometer as the controller input and for the measurement of response. In the third case, the control of the same 25.13 Hz mode is performed using the MFC patches as sensors and actuators, requiring an adjusted controller configuration. In all cases, the experiments follow the same procedure of shaker excitation, signal acquisition, controller activation, and post-processing of the measured data. In the fourth case, the mode at 25.13 Hz was excited using as a dSPACE controller as the control unit.

4.1. CASE 1: PURE-TONE SINE 129 HZ—Vibrometer as Input

The objective of this experiment is to control a disturbance at 129 Hz, that excites the 8th mode, close to its natural frequency at 132 Hz. The Simulink block diagram with the transfer function is shown in Figure 14.

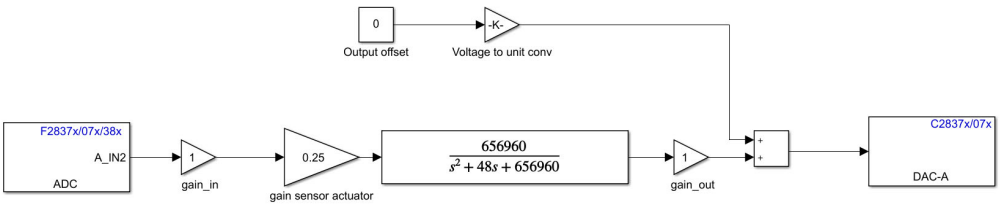

Figure 14. Simulink block diagram of the control scheme for the mode at 129 Hz.

The plate was excited through the shaker with a pure-tone sine wave at 129 Hz using an input signal ranging from −0.5 V to +0.5 V and loading was performed for a duration of 16 s to avoid transient responses after the controller was switched on, and the experimental results were post-processed. The time-domain analysis of the laser

vibrometer measurements shows a significant reduction in vibration velocity when the controller is active. With the controller switched off, the measured velocity was 0.086 m/s, while activating the controller reduced the velocity to 0.038 m/s. This corresponds to an approximate 55.8% reduction in vibration velocity in the time domain. Further analysis in the frequency domain was conducted using the Power Spectral Density (PSD). When the controller was inactive, the PSD amplitude was −13.53 dB, whereas activating the controller reduced the amplitude to −19.39 dB. This change corresponds to an amplitude reduction of approximately 6 dB, as illustrated in the PSD comparison shown in Figure 15.

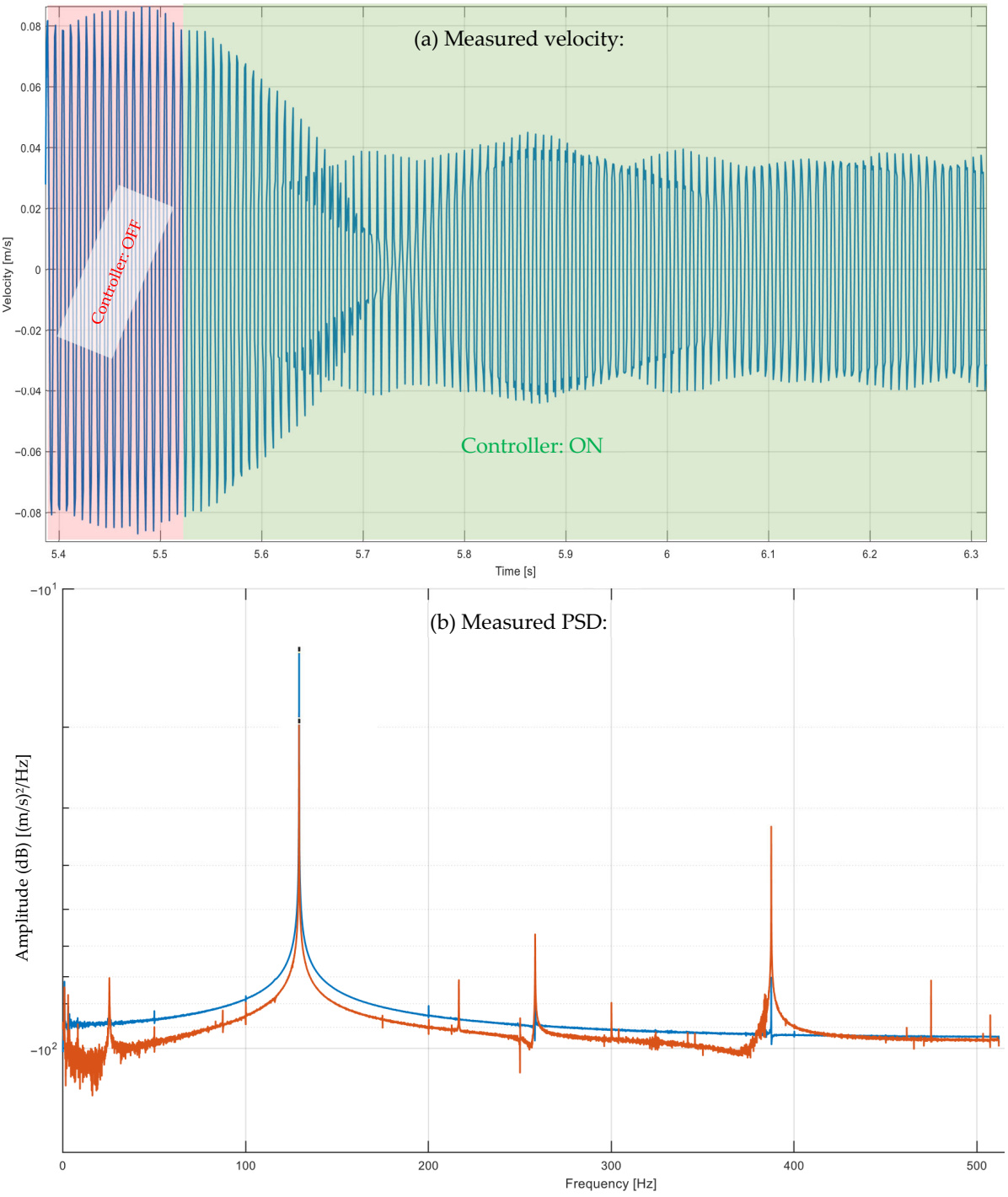

Figure 15. Velocity (**a**) and PSD (**b**) results measured by vibrometer during deactivated (blue) and activated (orange) controller phases at 129 Hz (case 1).

4.2. CASE 2: PURE-TONE SINE 25.13 HZ—Vibrometer as Input

In this experiment, the controller is set up to reduce the excitation around the mode at 25.13 Hz, where the controller transfer function was adjusted accordingly. The Simulink block diagram with the transfer function is shown in Figure 16.

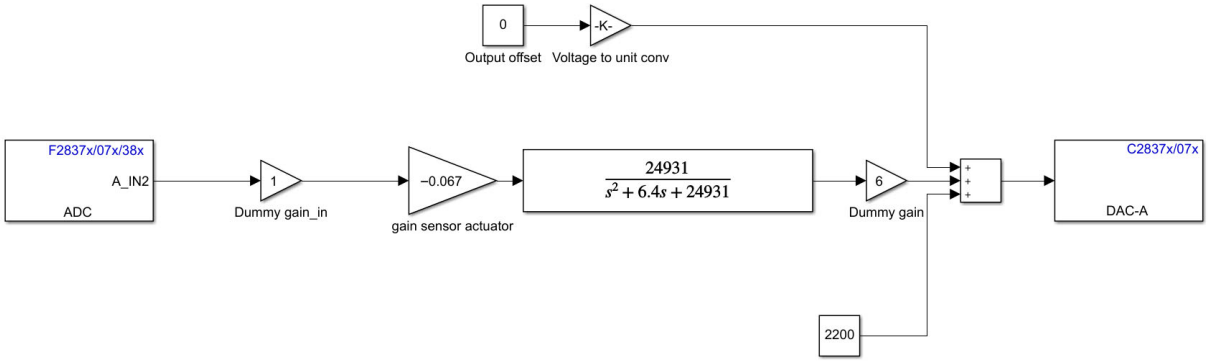

Figure 16. Simulink block diagram of the control scheme for the mode at 25.13 Hz—with the vibrometer as input.

The shaker was excited with a pure-tone sine wave at 25.13 Hz using an input signal ranging from −0.8 V to +0.8 V. Time-domain analysis of the laser vibrometer measurements indicates a substantial reduction in vibration velocity when the controller is active. With the controller switched off, the measured velocity was 0.078 m/s, while activating the controller reduced the velocity to 0.018 m/s. This corresponds to a vibration velocity reduction of approximately 76.9% in the time domain. Frequency-domain analysis was performed using Power Spectral Density (PSD), which shows that the input signal from the shaker exhibited a PSD amplitude in the response point of −12.73 dB, whereas the vibrometer output signal showed a reduced PSD amplitude of −25.56 dB when the controller was active. This change represents an amplitude reduction of approximately 13 dB, as illustrated in the PSD comparison shown in Figure 17.

4.3. CASE 3: PURE-TONE SINE 25.13 HZ—MFC Patch as Input

The objective of this experiment is to control an excitation close to the mode at 25.13 Hz, using an MFC patch as the sensor and actuator. The controller transfer function was adjusted accordingly, as seen in Figure 18.

The shaker was excited with a pure-tone sine wave at 25.13 Hz using an input signal ranging from −0.8 V to +0.8 V. As in the previous case, signal acquisition was initiated and the controller was switched on. Time-history analysis of the laser vibrometer measurements shows a clear reduction in vibration velocity when the controller is active. With the controller switched off, the measured velocity was 0.067 m/s, while activating the controller reduced the velocity to 0.018 m/s. This corresponds to a vibration velocity reduction of approximately 73.1% in the time domain. Frequency-domain analysis was performed using Power Spectral Density (PSD): without control, a PSD amplitude of −15.28 dB is measured, whereas the vibrometer output signal showed a reduced PSD amplitude of −27.04 dB when the controller was active. This difference represents an amplitude reduction of approximately 12 dB, as illustrated in the PSD comparison shown in Figure 19.

To better evaluate the results and the performances of this study, an additional experimental test case was conducted, case 4, in which the MCU was replaced with a dSPACE real-time control platform. The shaker was excited using a pure-tone sinusoidal signal at 25.13 Hz. When the controller was switched off, the measured voltage amplitude was 0.56 V, seen in Figure 20. Upon activating the controller, the voltage decreased to 0.21 V, demonstrating a significant attenuation of the response. This reduction corresponds to

an approximate 62.5% decrease in voltage responses in the time domain. Moreover, the control performance achieved using the MCU was found to be comparable to that obtained with the dSPACE system, thereby demonstrating the applicability and effectiveness of the MCU for real-time vibration control implementations.

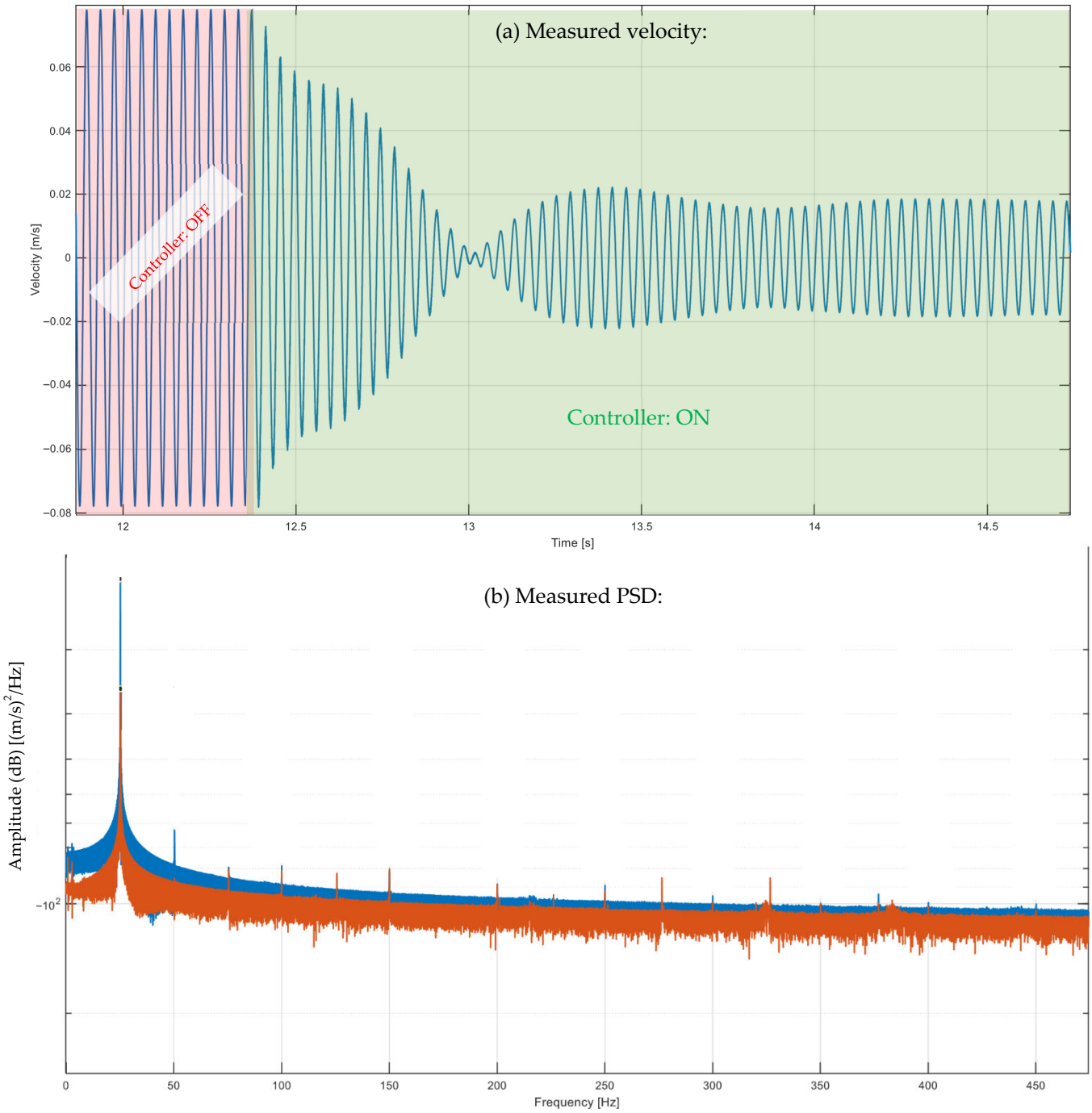

Figure 17. Velocity (**a**) and PSD (**b**) results measured by vibrometer during deactivated (blue) and activated (orange) controller phases at 25.13 Hz (case 2).

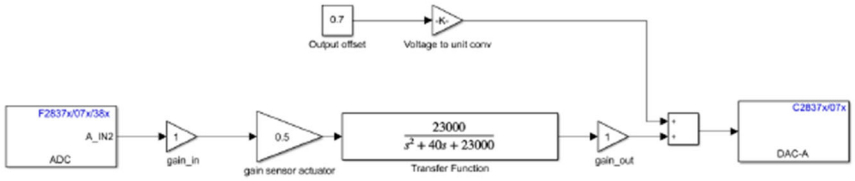

Figure 18. Simulink block diagram of the control scheme for the mode at 25.13 Hz—with the MFC patch as input.

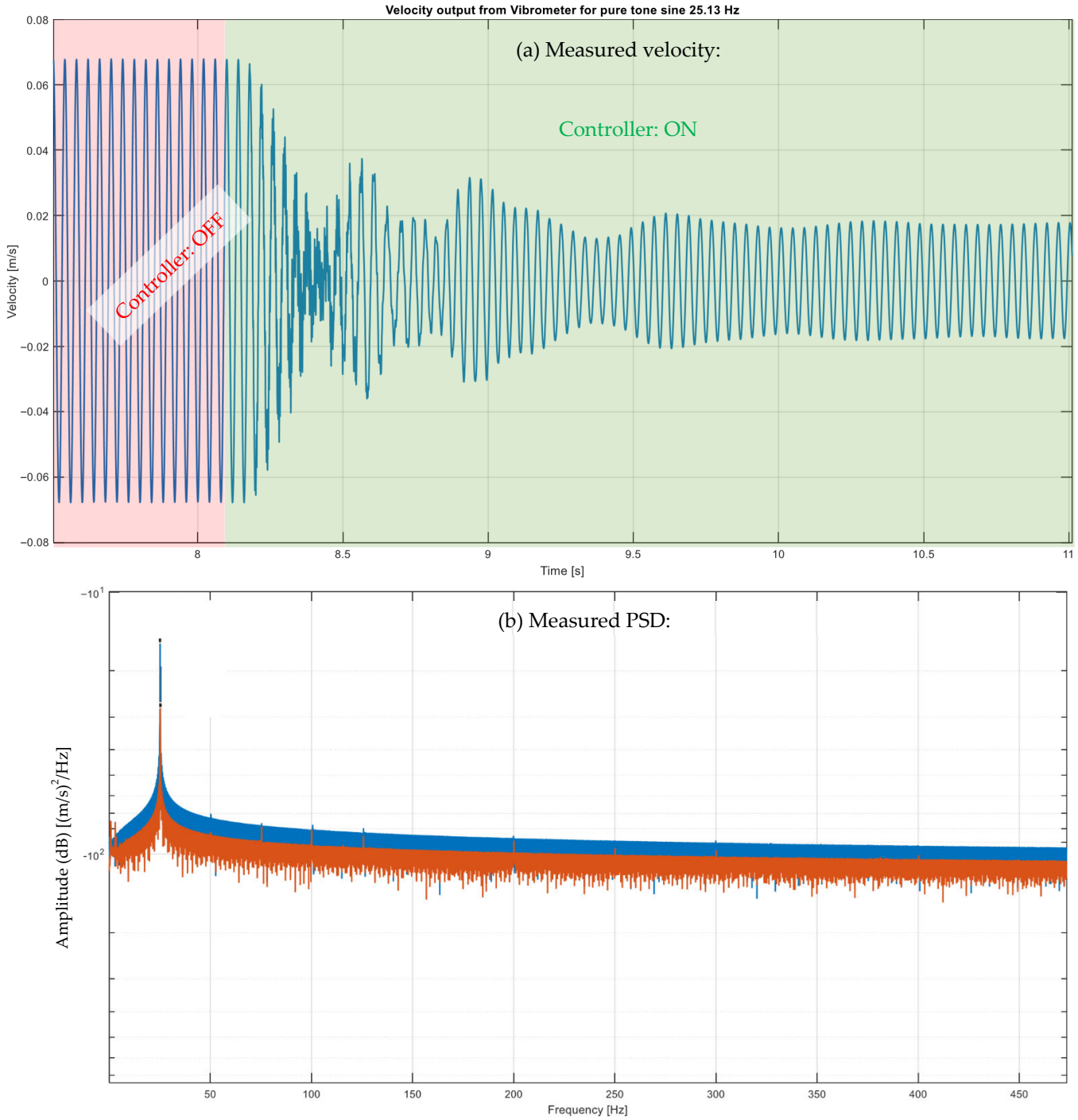

Figure 19. Velocity (**a**) and PSD (**b**) results measured by MFC patch during deactivated (blue) and activated (orange) controller phases at 25.13 Hz (case 3).

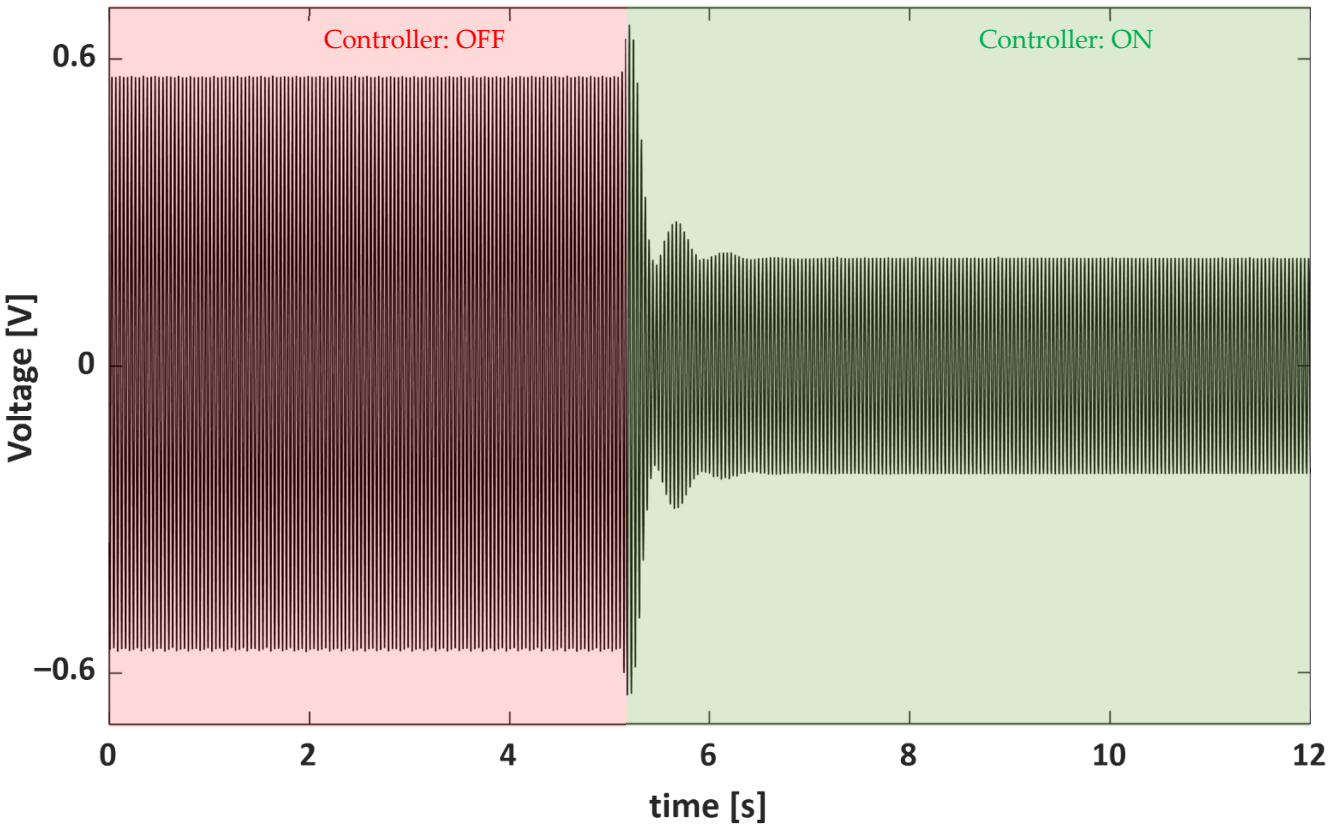

Figure 20. Time-history responses measured by MFC patch and controlled by dSPACE during deactivated and activated controller phases at 25.13 Hz.

5. Discussion

The experimental results demonstrate that a microcontroller-based implementation of positive position feedback can achieve a substantial attenuation of vibration in a composite honeycomb sandwich plate, even under the strict constraints imposed by embedded hardware. The observed reduction of approximately 74% in velocity amplitude and about 12 dB in PSD for the first flexural mode (25.13 Hz) confirms that the proposed control architecture is able to inject effective modal damping despite the limited ADC resolution, DAC range, and computational resources of the MCU. From a practical standpoint, this is a nontrivial result: it shows that the gap between laboratory-grade real-time platforms (such as dSPACE) and low-cost embedded controllers can be narrowed significantly with careful system-level design.

When interpreted in the context of previous studies, the achieved attenuation is consistent with, and in some cases comparable to, results obtained using more complex or computationally demanding platforms. Earlier works on PPF-based control of plates and beams implemented on dSPACE or similar DAQ systems typically report attenuation levels in the range of 60–90%, depending on modal separation and actuator authority. The present results fall within this envelope, reinforcing the idea that the control law itself—rather than the computational sophistication of the hardware—is the dominant factor for narrowband, modal vibration suppression. This aligns with findings in the literature that emphasize the robustness and spillover-resistant nature of PPF for lightly damped structures with well-separated modes.

A critical aspect highlighted by the experiments is the role of signal conditioning and hardware integration. The necessity of custom analog circuits to scale and shift sensor signals into the ADC range, and to properly drive the high-voltage amplifier for the MFC

actuators, emerges as a decisive factor in ensuring stability and performance. Inadequate conditioning would have amplified quantization noise or introduced offsets that could severely degrade control effectiveness. This observation corroborates earlier studies that stress how embedded AVC performance depends as much on analog front-end design as on the digital controller itself.

The choice of MFC patches as collocated or near-collocated sensor–actuator pairs also proved effective. Their high force capability, low mass, and compatibility with surface bonding make them particularly suitable for lightweight composite structures. The experimental attenuation confirms that, when placed in regions of high modal strain energy (identified through modal analysis and FEM), even a single actuator–sensor pair can exert sufficient authority over a targeted mode. This result supports the broader consensus in the literature on optimal placement strategies and validates the practical usefulness of modal strain energy as a guiding criterion.

It is worthwhile to observe that the present approach is effective under pure-tone harmonic excitation, which is a common scenario when the excitation source is a rotating machine (aerospace turbines, wind turbines, reciprocal machineries and engines, powerplants); on the other hand, other real scenarios, like wind-induced vibrations, ocean waves, or earthquakes, are typically characterized by randomness; in such cases there is no evidence of good performance by the PPF. Moreover, PPF is inherently a narrowband controller, and its performance is strongly tied to accurate tuning of the compensator frequency. Frequency shifts due to nonlinear effects [50], temperature variations [51], or boundary-condition changes could therefore reduce effectiveness. While PPF has been shown to tolerate weak nonlinearities, more severe nonlinear behavior or closely spaced modes would likely require adaptive or observer-based strategies, as suggested in more recent studies.

The experimental analyses developed in this work are intentionally focused on the harmonic forcing close to the selected resonance, which is the primary use-case for resonant PPF control in rotating machinery contexts. While broadband disturbance rejection is not the principal objective of a resonant controller, the strong high-frequency roll-off of the PPF filter (≈ -40 dB/oct beyond cutoff) is beneficial to mitigate spillover effects. Broadband excitation testing is therefore positioned as a complementary validation step when the intended application involves wideband forcing.

An important feature of the control proposed in this paper is the scalability; this work proves the effectiveness of a SISO control of a single mode. Extending this framework to multiple modes or to MIMO configurations is feasible in principle, but it raises additional challenges related to spillover, interaction between controllers, and computational load. Although the selected MCU has sufficient resources to handle multiple second-order compensators, careful tuning and possibly decentralized or decoupled control strategies would be required to maintain robustness.

In a broader context, the findings reinforce a key idea emerging in recent AVC research: effective vibration control does not necessarily require high-end hardware, but rather an intelligent co-design of structure, sensors, actuators, control law, and embedded implementation. The present study adds experimental evidence that microcontroller-based AVC is a viable and attractive solution for automotive and aerospace applications, where constraints on mass, volume, power consumption, and cost are often more restrictive than computational limits.

6. Conclusions

This paper proves the feasibility of implementing positive position feedback-based active vibration control on a composite honeycomb sandwich plate using a low-cost mi-

crocontroller platform. The present work demonstrated that effective modal vibration suppression could be achieved through an integrated embedded architecture combining microcontroller-based control and piezoelectric actuation on a composite structure. Indeed, the key contribution of this study is the experimental proof that a resource-constrained embedded microcontroller can deliver vibration attenuation performance comparable to conventional systems.

By integrating Macro Fiber Composite patches as sensor–actuator pairs with appropriate analog signal conditioning, the proposed embedded control architecture was shown to effectively suppress the targeted flexible mode, despite limitations in ADC/DAC resolution and computational resources. The results confirm that, for narrowband vibration suppression, control performance is primarily dictated by system-level design and controller tuning, rather than by the use of high-end real-time hardware.

The study also highlighted practical considerations for embedded active vibration control, including the importance of optimal actuator placement based on modal strain energy and robust hardware integration. Although the experiments were conducted on a single specimen configuration and focused on single-mode control under harmonic excitation, the findings provide a strong basis for extending the approach to multi-modal and multi-input–multi-output configurations, as well as to more realistic excitation scenarios. Overall, the work supports the viability of microcontroller-based active vibration control as a lightweight, cost-effective solution for automotive and aerospace applications.

Author Contributions: Conceptualization, A.Z. and F.P.; Methodology, A.Z., M.M. and F.P.; Software, A.Z., M.M. and E.B.; Validation, A.Z., M.M., E.B. and F.P.; Formal analysis, A.Z., M.M. and F.P.; Investigation, A.Z., M.M., E.B. and F.P.; Resources, A.Z. and F.P.; Data curation, A.Z., M.M., E.B. and F.P.; Writing—original draft, A.Z., M.M., E.B. and F.P.; Writing—review & editing, A.Z., M.M. and F.P.; Visualization, A.Z., M.M., E.B. and F.P.; Supervision, A.Z. and F.P.; Project administration, A.Z. and F.P.; Funding acquisition, A.Z. and F.P. All authors have read and agreed to the published version of the manuscript.

Funding: This research was funded by NATO grant SPS program, project G6176 "Composite Metamaterials for Aerospace Structures—CoMetA" (G6176).

Data Availability Statement: The original contributions presented in this study are included in the article. Further inquiries can be directed to the corresponding author.

Conflicts of Interest: The authors declare no conflict of interest.

References

1. Lee, Y.L.; Kim, D.H.; Park, J.S.; Hong, S.B. Vibration reduction simulations of a lift-offset compound helicopter using two active control techniques. *Aerosp. Sci. Technol.* **2020**, *106*, 106181. [CrossRef]
2. Liu, W.; Liu, W.; Zhou, M.; Tang, L.; Wang, Q.; Wen, Z.; Zhuang, Y.; Xiaojing, Y. An active vibration control method based on energy-fuzzy for cantilever structures excited by aerodynamic loads. *Chin. J. Aeronaut.* **2021**, *34*, 224–235. [CrossRef]
3. Balakrishna, S.; Houlden, H.; Butler, D.; White, R. Development of a Wind Tunnel Active Vibration Reduction System. In *Proceedings of the 45th AIAA Aerospace Sciences Meeting and Exhibit, Reno, NV, USA, 8-11 January 2007*; AIAA 2007-961; American Institute of Aeronautics and Astronautics: Reston, VA, USA, 2007; pp. 1–12. [CrossRef]
4. Ma, J.; Lu, Y.; Su, T.; Guan, S. Experimental research of active vibration and noise control of electrically controlled rotor. *Chin. J. Aeronaut.* **2021**, *34*, 106–118. [CrossRef]
5. Oveisi, A.; Nestorović, T.; Montazeri, A. Frequency Domain Subspace Identification of Multivariable Dynamical Systems for Robust Control Design. *IFAC-PapersOnLine* **2018**, *51*, 990–995. [CrossRef]
6. Wang, Z.; Keogh, P. Active Vibration Control for Robotic Machining. In *Proceedings of the ASME 2017 International Mechanical Engineering Congress and Exposition, Tampa, FL, USA, 3–9 November 2017*; American Society of Mechanical Engineers: New York, NY, USA, 2018; 6p. [CrossRef]

7. Jiang, H.; Long, X.; Meng, G. Active Vibration Control for Milling Processes. In *Proceedings of the ASME 2010 International Mechanical Engineering Congress and Exposition, Vancouver, BC, Canada, 12–18 November 2010*; American Society of Mechanical Engineers: New York, NY, USA, 2012; Volume 8, pp. 947–955. [CrossRef]
8. Ying, Z.G.; Ruan, Z.G.; Ni, Y.Q. Response Adjustability Analysis of Partial and Ordinary Differential Coupling System for Visco-Elastomer Sandwich Plate Coupled with Distributed Masses under Random Excitation via Spatial Periodicity Strategy. *Symmetry* **2022**, *14*, 1794. [CrossRef]
9. Takács, G.; Zometa, P.; Findeisen, R.; Rohal Ilkiv, B. Embedded Model Predictive Vibration Control on Low-End 8-bit Microcontrollers via Automatic Code Generation. In Proceedings of the 23rd International Congress on Sound & Vibration ICSV23, Athens, Greece, 10–14 July 2016; pp. 1–8.
10. Batista, G.; Takács, G.; Rohal'-Ilkiv, B. Application Aspects of Active-set Quadratic Programming in Real-time Embedded Model Predictive Vibration Control*. *IFAC-PapersOnLine* **2017**, *50*, 11625–11631. [CrossRef]
11. Hamed, Y.S.; Kandil, A.; Machado, J.T. Utilizing Macro Fiber Composite to Control Rotating Blade Vibrations. *Symmetry* **2020**, *12*, 1984. [CrossRef]
12. Zippo, A.; Ferrari, G.; Amabili, M.; Barbieri, M.; Pellicano, F. Active vibration control of a composite sandwich plate. *Compos. Struct.* **2015**, *128*, 100–114. [CrossRef]
13. Oveisi, A.; Jeronimo, M.B.; Nestorović, T. Nonlinear observer-based recurrent wavelet neuro-controller in disturbance rejection control of flexible structures. *Eng. Appl. Artif. Intell.* **2018**, *69*, 50–64. [CrossRef]
14. Oveisi, A.; Nestorović, T. Robust nonfragile observer-based H_2/H_∞ controller. *J. Vib. Control* **2016**, *24*, 722–738. [CrossRef]
15. Bai, L.; Feng, Y.W.; Li, N.; Xue, X.F.; Cao, Y. Data-Driven Adaptive Iterative Learning Method for Active Vibration Control Based on Imprecise Probability. *Symmetry* **2019**, *11*, 746. [CrossRef]
16. Belkourchia, Y.; Azrar, L.; Zeriab, E.S.M. Hybrid optimization procedure and active vibration control of beams with piezoelectric patches. In *Proceedings of the 2018 4th International Conference on Optimization and Applications (ICOA), Mohammedia, Marocco, 26–27 April 2018*; IEEE: Piscataway, NJ, USA, 2018; pp. 1–7. [CrossRef]
17. Hasheminejad, S.M.; Oveisi, A. Active vibration control of an arbitrary thick smart cylindrical panel with optimally placed piezoelectric sensor/actuator pairs. *Int. J. Mech. Mater. Des.* **2016**, *12*, 1–16. [CrossRef]
18. Kurpa, L.; Pellicano, F.; Shmatko, T.; Zippo, A. Free Vibration Analysis of Porous Functionally Graded Material Plates with Variable Thickness on an Elastic Foundation Using the R-Functions Method. *Math. Comput. Appl.* **2024**, *29*, 10. [CrossRef]
19. Pellicano, F.; Zippo, A. Ghost hammering in a randomly excited nonlinear dynamical system. *Chaos Solitons Fractals* **2025**, *199*, 116855. [CrossRef]
20. Aktaş, K.G.; Esen, İ. Dynamic Response Analysis and Active Vibration Control of the Smart Sandwich Composite Plate With FGM Core Layers and MIMO FGPM Actuators and Sensors. *Int. J. Mech. Syst. Dyn.* **2025**, *5*, 3–19. [CrossRef]
21. Wen, X.; Guo, J.; Yan, P.; Li, S. Active Vibration Rejection of Smart Thin Plate Based on Predictive Composite Observer. *IEEE Trans. Ind. Electron.* **2025**, *72*, 14182–14191. [CrossRef]
22. Umar, H.M.; Zhang, L.; Yu, R.; Gao, Z. Improved active vibration control of a cantilever beam using MFC actuators with Hammerstein model-based hysteresis modeling and VSS-FxLMS control algorithm. *J. Low Freq. Noise Vib. Act. Control* **2025**, *44*, 1169–1186. [CrossRef]
23. Sun, X.G.; Chi, W.C.; Wang, Y.Q. Linear active disturbance rejection control algorithm for active vibration control of piezo-actuated beams: Theoretical and experimental studies. *Thin-Walled Struct.* **2024**, *199*, 111782. [CrossRef]
24. Gulan, M.; Takács, G.; Olaru, S. Lifted Explicit Interpolating Control for Low-End Embedded Microcontrollers: An Active Vibration Control Case Study. *IFAC-PapersOnLine* **2024**, *58*, 576–581. [CrossRef]
25. Iarriccio, G.; Zippo, A.; Eskandary-Malayery, F.; Ilanko, S.; Mochida, Y.; Mace, B.; Pellicano, F. Tunable High-Static-Low-Dynamic Stiffness Isolator under Harmonic and Seismic Loads. *Vibration* **2024**, *7*, 829–843. [CrossRef]
26. Zippo, A.; Iarriccio, G.; Molaie, M.; Pellicano, F. Novel Nonlinear Suspension Based on Concept of Origami Metastructures: Theoretical and Experimental Investigations. *Vibration* **2024**, *7*, 1126–1155. [CrossRef]
27. Huang, Y.; Zhou, J.; Shen, L.; Li, H.; Lin, Z.; Zhang, Z. A novel active vibration suppression device based on momentum wheel and pendulum-tuned mass damper. *J. Low Freq. Noise Vib. Act. Control* **2025**, *45*, 566–580. [CrossRef]
28. Jian, Y.; Hu, G.; Tang, L.; Shen, Y.; Zhan, Y.; Aw, K. Adaptive piezoelectric metamaterial beam: Autonomous attenuation zone adjustment in complex vibration environments. *Smart Mater. Struct.* **2023**, *32*, 105023. [CrossRef]
29. Soleimanian, S.; Petrone, G.; Franco, F.; De Rosa, S.; Kołakowski, P. Semi-active vibro-acoustic control of vehicle transmission systems using a metal rubber-based isolator. *Appl. Acoust.* **2024**, *217*, 109861. [CrossRef]
30. Bloemers, T.; Leemrijse, S.; Preda, V.; Boquet, F.; Oomen, T.; Tóth, R. Vibration Control Under Frequency-Varying Disturbances With Application to Satellites. *IEEE Trans. Control Syst. Technol.* **2024**, *32*, 1983–1994. [CrossRef]
31. Cui, M.; Tang, W.; Han, Y.; Li, Z. Smart Active Vibration Control System Using Piezoelectric Materials. In *Proceedings of the 2020 Chinese Control And Decision Conference (CCDC), Hefei, China, 22–24 August 2020*; IEEE: Piscataway, NJ, USA, 2020; pp. 2611–2615. [CrossRef]

32. Balas, M.J. Active control of flexible systems. *J. Optim. Theory Appl.* **1978**, *25*, 415–436. [CrossRef]
33. Joshi, S.M. *Control of Large Flexible Space Structures*; Springer: Berlin/Heidelberg, Germany, 1989. [CrossRef]
34. Poh, S.; Baz, A. Active control of a flexible structure using a modal positive position feedback controller. *J. Intell. Mater. Syst. Struct.* **1990**, *1*, 273–288. [CrossRef]
35. Fanson, J.L.; Caughey, T.K. Positive position feedback control for large space structures. *AIAA J.* **1990**, *28*, 717–724. [CrossRef]
36. Goh, C.J.; Caughey, T.K. On the stability problem caused by finite actuator dynamics in the collocated control of large space structures. *Int. J. Control* **1985**, *41*, 787–802. [CrossRef]
37. Hagood, N.W.; von Flotow, A. Damping of structural vibrations with piezoelectric materials and passive electrical networks. *J. Sound Vib.* **1991**, *146*, 243–268. [CrossRef]
38. Moheimani, S.O.R.; Fleming, A.J. Feedback Control of Structural Vibration. In *Piezoelectric Transducers for Vibration Control and Damping*; Springer: London, UK, 2006. [CrossRef]
39. Preumont, A. *Vibration Control of Active Structures: An Introduction*, 4th ed.; Springer: Berlin/Heidelberg, Germany, 2018. [CrossRef]
40. Mahmoodi, S.N.; Ahmadian, M. Active vibration control with modified positive position feedback. *J. Dyn. Syst. Meas. Control* **2009**, *131*, 041002. [CrossRef]
41. Rew, K.-H.; Han, J.-H.; Lee, I. Multi-Modal Vibration Control Using Adaptive Positive Position Feedback. *J. Intell. Mater. Syst. Struct.* **2002**, *13*, 13–22. [CrossRef]
42. Clark, R.L.; Saunders, W.R.; Gibbs, G.P. *Adaptive Structures: Dynamics and Control*; John Wiley & Sons: New York, NY, USA, 1998; ISBN 13 978-0471122623.
43. Baz, A.; Poh, S. Performance of an active control system with piezoelectric actuators. *J. Sound Vib.* **1988**, *126*, 327–343. [CrossRef]
44. Fuller, C.R.; Elliott, S.J.; Nelson, P.A. *Active Control of Vibration*; Academic Press: San Diego, CA, USA, 1996; ISBN 0122694414, 9780122694417.
45. Fleming, A.J.; Moheimani, S.O.R. Control orientated synthesis of high-performance piezoelectric shunt impedances for structural vibration control. *IEEE Trans. Control Syst. Technol.* **2005**, *13*, 98–112. [CrossRef]
46. Vlase, S.; Itu, C. The Properties of Structures with Two Planes of Symmetry. *Symmetry* **2024**, *16*, 1075. [CrossRef]
47. Yang, Y.; Zhang, Y.; Tan, X. Review on vibration-based structural health monitoring techniques and technical codes. *Symmetry* **2021**, *13*, 1998. [CrossRef]
48. Zippo, A.; Pellicano, F.; Iarriccio, G. Microcontroller design for active vibration control. *Mater. Res. Proc.* **2023**, *26*, 479–484. [CrossRef]
49. *TMS320F28379D*; Technical Reference Manual. Texas Instruments: Dallas, TX, USA, 2024. Available online: https://www.ti.com/product/TMS320F28379D (accessed on 17 February 2026).
50. Pellicano, F.; Mastroddi, F. Nonlinear dynamics of a beam on elastic foundation. *Nonlinear Dyn.* **1997**, *14*, 335–355. [CrossRef]
51. Zippo, A.; Barbieri, M.; Iarriccio, G.; Pellicano, F. Nonlinear vibrations of circular cylindrical shells with thermal effects: An experimental study. *Nonlinear Dyn.* **2020**, *99*, 373–391. [CrossRef]